ADVANCED ENERGY MATERIALS

Supporting Information

for *Adv. Energy Mater.*, DOI 10.1002/aenm.202300506

Effect of Hole Transport Materials and Their Dopants on the Stability and Recoverability of Perovskite Solar Cells on Very Thin Substrates after 7 MeV Proton Irradiation

*Shi Tang, Stefania Peracchi, Zeljko Pastuovic, Chwenhaw Liao, Alan Xu, Jueming Bing, Jianghui Zheng, Md Arafat Mahmud, Guoliang Wang, Edward Dominic Townsend-Medlock, Gregory J. Wilson, Girish Lakhwani, Ceri Brenner, David R. McKenzie and Anita W. Y. Ho-Baillie**

Supporting Information

Effect of Hole Transport Materials and their Dopants on the Stability and Recoverability of Perovskite Solar Cells on Very Thin Substrates after 7 MeV Proton Irradiation

*Shi Tang, Stefania Peracchi, Zeljko Pastuovic, Chwenhaw Liao, Alan Xu, Jueming Bing, Jianghui Zheng, Md Arafat Mahmud, Guoliang Wang, Edward Dominic Townsend-Medlock, Gregory J. Wilson, Girish Lakhwani, Ceri Brenner, David R. McKenzie, and Anita W.Y. Ho-Baillie**

Experimental Procedures:

Materials: SnO_2 (tin (IV) oxide, 15% in H_2O colloidal dispersion) precursor was purchased from Alfa Aesar. Cesium iodide (CsI), N, N-dimethylformamide (DMF), n-methyl-2-pyrrolidone (NMP), Chlorobenzene, Lithium bis(trifluoromethanesulfonyl)imide (LITFSI), Tris(pentafluorophenyl)borane (TPFB), were obtained from Sigma-Aldrich. Lead Iodide (PbI_2) was purchased from TCI. Formamidinium iodide (FAI) and tris(2-(1H-pyrazol-1-yl)-4-tert-butylpyridine)cobalt(III) tri[bis(trifluoromethane)sulfonimide] (FK209) were obtained from Greatcell Solar Materials. Spiro-OMeTAD, PTAA and C8BTBT were purchased from Derthon Optoelectronic Materials Science Technology Co Ltd. DC 93-500 space grade encapsulant was obtained from Dow-Corning.

Precursor preparation: tin (IV) oxide colloidal dispersion was diluted with deionized water to 2.67 wt.%. $Cs_{0.15}FA_{0.85}PbI_3$ precursor was prepared by dissolving 0.24 M CsI, 1.36 M FAI, 1.73 M PbI_2 in 900 µL DMF and 100 µL NMP.

For preparing the Spiro-OMeTAD(LiTFSI) precursor, solution was prepared that consisted of 90 mg Spiro-MeOTAD, 23 µL LiTFSI (520 mg/mL) stock solution, 12.5 µL FK209 (300 mg/mL) stock solution, 39.5 µL tBP and 1 mL chlorobenzene.

For preparing the Spiro-OMeTAD(TPFB) precursor, solution was prepared that consisted of 90 mg Spiro-MeOTAD, 10.8 mg TPFB, 12.5 µL FK209 (300 mg/mL) stock solution, 39.5 µL tBP and 1 mL chlorobenzene.

For preparing the PTAA(LiTFSI) or C8BTBT(LiTFSI) precursor, PTAA or C8BTBT was dissolved in chlorobenzene at 20 mg/mL with 2.4 mg LiTFSI as dopant .

For preparing the PTAA(TPFB) or C8BTBT(TPFB) precursor, PTAA or C8BTBT was dissolved in chlorobenzene at 20 mg/mL with 2.4 mg TPFB as dopant.

For the fabrication of PTAA:Spiro and PTAA:C8BTBT layers, PTAA precursor were mixed with Spiro-OMeTAD or C8BTBT precursor in a volume ratio of 1:1, respectively prior to deposition.

Preparation of sapphire substrate: 2-inch 175 µm double side polished sapphire wafers were coated with AZ1505 photoresist at 3000 rpm for 30s. The sapphire substrates were then cut into 2 cm × 2 cm using a dicing saw. The 2×2 cm^2 sapphire substrates were sequentially cleaned in acetone, 2.0 wt.% detergent, deionized water, and isopropanol for 20 minutes. After cleaning, the sapphire substrates were dried by N_2 and 40 nm Al_2O_3 was deposited using a Picosun ALD system. ITO was sputtered onto the sapphire substrate at a power of 30 W from a 2-inch ITO (In_2O_3/SnO_2 90/10 wt %) target.

Fabrication of perovskite solar cells: ITO substrates were placed in a UV-Ozone cleaner for 15 minutes. A 2.67 wt.% SnO_2 solution was spun onto the ITO substrates at 4500 rpm for 30 s. The SnO_2-coated ITO substrates were annealed on a hotplate at 150 °C for 30 minutes. After a 30-minute UV-Ozone treatment, the SnO_2-coated ITO substrates were transferred into an N_2-

filled glovebox with O_2 and H_2O below 1 ppm. 30 µL 1.6 M perovskite precursor solution was delivered onto the substrates and spin-coated at 2000 rpm for 10 s and 6000 rpm for 30 s. After 17 s of the start, an N_2 blow (6 bar, 100L/min) was applied to the substrate at ~0.4 cm over the substrates. Afterwards, the substrates were annealed at 100 °C for 10 minutes on a hot plate. HTM solutions were spin-coated onto the perovskite surface at 4500 rpm for 30 s without any further annealing. 100 nm Au was thermally evaporated under 1×10^{-5} Pa with a metal mask to define the active area of a PSC.

Encapsulation of perovskite solar cells: the base and curing agent from the DC 93-500 encapsulant were mixed at a weight ratio of 10:1. The mixture was blade coated onto a 125-µm polyimide film (1.2 cm × 1 cm) and the polyimide film was then attached to the top of PSC with the encapsulant in direct contact with the PSC and was left in a compressed dry air box for 24 hours for curing. Metal masks with apertures (3-mm diameter circles) were then attached to the PSCs to define the irradiation areas.

Proton irradiations: PSC samples were irradiated by the raster scanning proton microbeam at the Australia's Nuclear Science and Technology Organization (ANSTO) Centre for Accelerator Science. 1MeV, is produced by the 6 MeV SIRIUS tandem accelerator. 7 MeV or 10MeV proton microbeam is produced by the 10 MV Van de Graaff ANTARES Heavy Ion Nuclear Microprobe instrument. The high-energy proton beam is filtered and collimated using a pair of automated high precision double slits with micrometre accuracy, scanned in 2D by dipole electromagnets and focused using a system of quadrupole electromagnets lenses. The high precision slits allow for excellent adjustment of a beam current in the order of pA, or particle rate, and define the beam object size that is de-magnified to a sub-micron image size using the quadrupole lens system. For devices under tests, PSCs were mounted onto sample holders as shown in Figure S3. Apertures were used to separate PSCs for different fluence

exposures: 10^{11}, 10^{12} and 10^{13} protons/cm^2. For reference PSC with no proton exposure, Cu tape (in 3 layers) was used for masking. The pixel dwell time was set to 450 µs to complete one full scan of the target area in 30 s. Consecutive multiple scans were performed on individual PSCs to deliver the desired fluence with the current and exposure time specified in Table S2.

Thermal vacuum anneal for radiated perovskite solar cells: was carried out in a (Key Factor. Inc Hong Kong) 25L 304 SS thermal vacuum chamber connected to an Edwards T-Station 85, within which the proton irradiated sample was placed onto a coalesced copper sample holder and pumped down to 1×10^{-5} Pa in ~30 minutes. The temperature was then ramped up from room temperature to 80 ºC at a ramp rate of 5 ºC/min and held at 80 ºC for 30 mins. The chamber was then cooled down naturally to room temperature in approximately 3 hours. After cooling down the chamber was filled with high purity nitrogen and the sample was taken out.

Optical imaging: was taken with Olympus DSX510 under the backfield mode with a total magnification of 555x**.**

SEM imaging: was acquired using Zeiss Crossbeam 550XL using an accelerating voltage of 5kV and a working distance of 4.3 mm. During the SEM imaging, the substrates were connected to the sample holder via a copper clip to dissipate the surface charge.

Atomic force microscopy (AFM) and conductive-AFM (c-AFM): were obtained using a Bruker Icon AFM with SCM-PIT-V2 tip under PeakForce TUNA mode. The samples were connected to the holder via a copper clip, -1V voltages were applied to all samples and the scan rate was set to 0.996 Hz throughout the imaging.

UV-VIS spectra: were acquired using a Cary 500 with a 5-nm step and before measurement 0% and 100% calibrations were carried out.

Sheet resistance: was measured using a four-probe stage and a Keithley 2400 source measurement unit through the Van der Pauw method**.**

X-ray diffraction (XRD) patterns: were obtained using a PANalytical X'Pert X-ray diffractometer.

Current-voltage measurement: A Newport 94083 solar simulator was used as a light source and the spectra were calibrated with a reference Si solar cell with a KG5 window from Fraunhofer Institute for Solar Energy Systems. The current-voltage scanning was obtained from Tracer software (ReRa Solutions BV) from 1.3 V to -0.1 V with a 20-mV interval with a Keithley 2636B source measurement unit.

Temperature-dependent measurements: Irradiated samples were placed in a probe station (Key Factor. Inc Hong Kong) and each manipulator of the probe station was equipped with a true-kelvin probe (73APT-100K Kelvin Probe). The temperature was controlled and monitored by a Lakeshore 336 temperature controller.

For the temperature-dependent V_{OC}, PSC and a 4500K LED chip on board (COB) were placed inside the probe station and were connected to a Keithley 2636B source measurement unit through triaxial cables. One channel of the Keithley 2636B was used to power the LED, and the other was used for V_{OC} measurement.

Thermal admittance spectroscopy (TAS) was carried out using a Keysight E4990A impedance analyser (20Hz-10MHz with “Enhanced Measurement Speed” option). Before the measurement, the fixture was compensated through open and short compensation.

For deep level transient spectroscopy (DLTS), an HF2LI lock-in amplifier and Keysight 33522B pulse generator were used with a sampling frequency of 900 kHz with pulse -1 to 0 V for 100 ms. The transients were measured over 30 s and averaged with MATLAB-based software at a temperature range of 200-400K.

Depth-resolved X-ray photoelectron spectroscopy (XPS): was conducted using a ThermoFisher Scientific K-Alpha X-ray Photoelectron Spectrometer System with 72W monochromatic Al Kα (1486.6 eV) X-ray source. Before the measurement, the Au electrodes from the PSCs were mechanically peeled off with scotch tape. The etching was achieved by an Ar cluster ion beam and the estimated etching rate was 0.15 nm/s.

Table S1. Reported proton radiation tests on perovskite solar cells. Only results of the higher performing cells from this work are included in this table.

Energy	**Accumulated Fluence (p/cm^2)**	**Irradiated side**	**Device architecture**	**Before and after radiation**			**Ref**
				Irradiation conditions	**Efficiency***	**Estimated power to weight ratio (mW/g)$^>$**	
150 keV	10^{12} (3s) 10^{13} (33s) 10^{14} (333s) Flux at 3×10^{11} p cm^{-2}s^{-1}	Cell rear	Quartz (1mm)/ITO/TiO_2/$MAPbI_3$/P3HT/Au	as fabricated	4.8% average	18	1
				post 10^{12} p/cm^2	>4.8%×95%	>17	
				post 10^{13} p/cm^2	4.8%×80%	14	
				post 10^{14} p/cm^2	4.8%×70%	13	
50 keV	10^{12}	Cell rear	Quartz (1 mm)/ITO/c-NiO/$FAPbI_3$/PCBM/Ag	as fabricated	12.3%	45	2
				post radiation	7.4%	27	
50 keV	10^{12} (3.3s) to	Cell rear	Quartz (1mm)/ITO/c-TiO_2/mp-TiO_2/perovskite $MAPbI_3$:Cl/P3HT/Au	perovskite = $MAPbI_3$:Cl			3
				as	4.8%	18	

	10^{15} (3333s) Flux at 3×10^{11} p $cm^{-2}s^{-1}$			fabricated			
				post 10^{12} p/cm^2	4.8%	18	
				post 10^{13} p/cm^2	5.0%	19	
				post 10^{14} p/cm^2	5.3%	20	
				perovskite = $Cs_XFA_{0.85}MA_{0.15}Pb(I_{0.85}Br_{0.15})_3$			
				as fabricated	4.4%	17	
				post 10^{12} p/cm^2	4.6%	17	
				post 10^{13} p/cm^2	4.5%	17	
				post 10^{14} p/cm^2	3.5%	13	
				post 10^{15} p/cm^2	2.4%	9	
150 keV	10^{12} to 10^{15}	Cell rear	Quartz (1mm)/AZO/SnO_2/CsMAFAPbIBr/spiro-OMeTAD/Au	as fabricated	15%	57	4
				post 10^{12} p/cm^2	18%	68	
				post 10^{13} p/cm^2	14%	53	
				post 10^{14} p/cm^2	3%	11	
				post 10^{15} p/cm^2	0%	0	
50 keV	10^{13} to 10^{15}	Cell rear	Glass (2.2 mm)/FTO/c-TiO_2/mp-TiO_2/$Rb_{0.03}Cs_{0.05}FA_{0.83}MA_{0.17}Pb(I_{0.83}Br_{0.17})_3$/Spiro-OMeTAD/Au	as fabricated	18%-20%	33-36	5
				post radiation	?	?	
100 keV	10^{12}-10^{14} Flux at 5×10^{11} p $cm^{-2}s^{-1}$	Cell rear	Glass (2.2mm)/FTO/SnO_2/ $Cs_{0.01}MA_{0.01}FA_{0.98}PbI_3$/spiro-OMeTAD/Au	as deposited	~15.5%	~28	6
				post $2x10^{13}$ 100keV	~14.6%	~27	
				post $1x10^{14}$ 100keV	~3.1%	~5.7	
2 MeV				as deposited	~12.5%	~23	
				post	~12.5%	~23	

				$1x10^{14}$ 2MeV			
				post $1x10^{15}$ 2MeV	0%	0	
50keV	10^{10}-10^{12} Flux at 1×10^{9} to 4.7×10^{10} p $cm^{-2}s^{-}$	Cell rear	Glass (1.1mm)/ITO/polyTPD/PFN-Br/$FA_{0.8}Cs_{0.2}PbI_{2.4}Br_{0.6}Cl_{0.02}$/LiF/C60/$SnO_X$/ZTO/ITO/$Al_2O_3$ encapsulant	as fabricated	5.6%$^{+}$	21	7
				post 50keV	4.3%$^{+}$	16	
300 keV				as fabricated	5.8%$^{+}$	22	
				post 300keV	8.5%$^{+}$	32	
2.5 MeV				as fabricated	5.4%$^{+}$	21	
				post 2.5MeV	6.3%$^{+}$	24	
1MeV	8.6×10^{10}	Cell rear	Glass(2.2mm)/FTO/TiO_2/$MAPbI_3$/spiro-OMeTAD /Au	as fabricated	7.5%	14	8
				post 1 MeV	3.2%	5.8	
5MeV				as fabricated	7.5%	24	
				post 5 MeV	5.4%	9.8	
10 MeV				as fabricated	7.2%	13	
				post 10 MeV	7.0-7.2%	13	
150 keV	1×10^{15}	Cell rear	Glass(2.2mm)/FTO/TiO_2/ZrO_2/carbon loaded with $MAPbI_3$-AVA	as fabricated	13.0%	49	9
				post radiation	>12.9%	>48	
68 MeV	10^{13} (Flux at 1.68×10^{9} p $cm^{-2}s^{-1}$ for 101 min)	Front glass	Glass (1.1mm)/ITO/PEDOT:PSS/$MAPbI_3$/PCBM/BCP/Ag	as fabricated	12.1%	44	10
				post radiation	6 % or 8% if taking glass damage into account	22 or 30	
68 MeV	10^{13} (Flux at 1.68×10^{9} p $cm^{-2}s^{-1}$ for 101 min)	Front glass	Glass (1.1mm)/ITO/PEDOT:PSS/$MAPbI_3$/PC61BM/BCP/Ag	as fabricated	4.7%	17	11
				post radiation	5.7%	21	
20 MeV 68 MeV	10^{12}	Front quartz	Quartz (1mm)/ITO/PTAA/$Cs_{0.05}MA_{0.17}FA_{0.83}Pb(I_{0.83}Br_{0.17})_3$/C60/BCP/Cu	as fabricated	18.8%	71	12
				post	17.8%	67	

				radiation			
68MeV	10^{12} (Flux at 7×10^{8} p $s^{-1}cm^{-2}$ for 48 mins)	Front quartz	Quartz (1mm)/LiF/IZO/C60/SnO_2/$Cs_{0.05}(MA_{0.17}FA_{0.83})_{0.95}Pb(I_{0.83}Br_{0.17})_3$/PTAA/NiO/ZnO/CdS/Cu(In,Ga)Se_2/Mo	as fabricated	18.0%	67	13
				post radiation	14.9%	56	
			Quartz (1mm)/LiF/IZO/C60/SnO_2/$Cs_{0.05}(MA_{0.17}FA_{0.83})_{0.95}Pb(I_{0.83}Br_{0.17})_3$/PTAA/ITO/nc-$SiO_X$/(i)a-Si:H/c-Si/(p)a-Si:H/Al:ZnO/Ag	as fabricated	21.1%	79	
				post radiation	0.18%	0.67	
68 MeV	2×10^{12} and 1×10^{13} Flux at 1.68×10^{9} p $cm^{-2}s^{-1}$	Front quartz	Quartz (1mm)/ITO/polyTPD/PFN/ $FA_{0.6}Cs_{0.3}DMA_{0.1}PbI_{2.4}Br_{0.6}$/LiF/C60/PEIE/AZO/ITO/PEDOT:PSS/$FA_{0.75}Cs_{0.25}Sn_{0.5}Pb_{0.5}I_3$/C60/BCP/Au	as deposited	~15.6%$^{+}$	~59	14
				post $2x10^{12}$ radiation	~15.1%$^{+}$	~57	
				post $1x10^{13}$ radiation	~14.7%$^{+}$	~55	

7 MeV	1×10^{11} (average flux at 8.3×10^{8} p $cm^{-2}s^{-1}$ for 2 min) 1×10^{12} (average flux at 8.3×10^{9} p $cm^{-2}s^{-1}$ for 2 min) 1×10^{13} (average flux at 8.7×10^{9} p $cm^{-2}s^{-1}$ for 19 min)	Front sapphire	Sapphire (**0.175 mm**)/ITO/SnO_2/$Cs_{0.15}FA_{0.85}PbI_3$/ **HTM**/Au	HTM = PTAA(TPFB):Spiro(LiTFSI)			**This work**
				as fabricated	Average 16.3%	**230**	
				Post **TV**	Average 10.1%	**143**	
				post 10^{11}	Average 16.1%	**230**	
				post 10^{11} + **TV**$^{-}$	Average 9.3%	**133**	
				post 10^{12}	Average 12.3%	**170**	
				post 10^{12} + **TV**$^{-}$	Average 6.4%	**88**	
				post 10^{13}	Average 7.8%	**110**	
				post 10^{13} + **TV**$^{-}$	Average 3.0%	**42**	
				HTM = PTAA(TPFB)			
				as fabricated	Average 14.9%	**220**	
				Post TV	Average 13.9%	**205**	
				post 10^{11}	Average 13.7%	**200**	
				post 10^{11} + **TV**$^{-}$	Average **16.4**%	**237**	
				post 10^{12}	Average 12.1%	**180**	
				post 10^{12} + **TV**$^{-}$	Average **14.9**%	**222**	
				post 10^{13}	Average 8.5%	**120**	
				post 10^{13} + **TV**$^{-}$	Average **10.0**%	**141**	
				HTM = PTAA(TPFB):C8BTBT(TPFB)			
				as fabricated	Average 18.0%	**260**	
				Post TV	Average **18.2**%	**263**	
				post 10^{11}	Average 17.1%	**240**	
				post 10^{11} + **TV**$^{-}$	Average **17.2**%	**241**	
				post 10^{12}	Average 16.6%	**240**	
				post 10^{12} + **TV**$^{-}$	Average **16.9**%	**244**	
				post 10^{13}	Average 10.3%	**150**	
				post 10^{13} + **TV**$^{-}$	Average **11.9**%	**173**	

* Measured under AM 1.5G unless stated otherwise

[+] Measured under AM 0 unless stated otherwise

~ TV = thermal (80°C) vacuum anneal

> calculations do not include weight of encapsulations

Table S2. Sheet resistance (Ω/□) and root-mean-square (RMS) roughness ITO as a function of underlying Al_2O_3 buffer layer thickness.

Al_2O_3 buffer layer thickness (nm)	ITO			
	Sheet resistance (Ω/□)	RMS roughness (nm)	Transmittance (%)	
			Average (200-800 nm)	Maximum
0	23.1	1.8	72.4	83.5 (402 nm)
20	22.6	2.0	73.3	85.1 (402 nm)
40	21.2	1.9	73.6	87.7 (462 nm)
60	24.3	5.1	73.2	87.2 (462 nm)

Table S3. Parameters used for SRIM simulations.

Material	Density (g/cm^3)	Thickness (μm)
Sapphire	3.98	175
ITO	7.17	0.22
SnO_2	6.95	0.04
Perovskite ($Cs_{0.15}FA_{0.85}PbI_3$)	3.88-4.18	0.65
PTAA	1.00	0.02
Au	19.30	0.10

Table S4. Proton irradiation conditions for the delivery of three fluences to the PSCs under test.

Fluence (protons/cm^2)	Proton beam current (pA)	Exposure time (min)
10^{11}	10	2
10^{12}	100	2
10^{13}	100	19

Table S5. Trap parameters for the higher performing perovskite solar cells after 7 MeV proton irradiation and after additional thermal vacuum anneal

HTM	Accumulated Fluence	E_t (eV)	Defects density (cm^{-3})		N_A* (cm^{-3})	E_A (eV)
			Post 7MeV	Post 7MeV + TV		

	s (p/cm^2)		TAS	DLTS	TAS	DLTS	Post 7MeV	Post 7MeV + TV	Post 7MeV	Post 7MeV + TV
PTAA(TPFB):Spiro (LiTFSI)	0	E_V+0.31	7.3×10^{13}	2.9×10^{13}	3.4×10^{14}	1.8×10^{14}	6.1×10^{17}	8.9×10^{18}	1.57	1.54
		E_V+0.43		1.6×10^{15}		7.2×10^{16}				
	10^{11}	E_V+0.31	2.0×10^{15}	1.6×10^{15}	3.1×10^{15}	4.8×10^{15}	1.2×10^{17}	1.1×10^{19}	1.53	1.49
		E_V+0.43		3.2×10^{15}		6.9×10^{17}				
	10^{12}	E_V+0.31	7.7×10^{15}	1.1×10^{16}	1.9×10^{16}	4.1×10^{18}	1.3×10^{17}	3.6×10^{19}	1.42	1.37
		E_V+0.43		3.3×10^{16}		7.5×10^{18}				
	10^{13}	E_V+0.31	1.0×10^{16}	7.2×10^{15}	1.3×10^{17}	1.1×10^{18}	1.2×10^{17}	4.5×10^{19}	1.36	1.32
		E_V+0.43		2.0×10^{16}		5.4×10^{18}				
		E_V+0.68		5.0×10^{15}		8.7×10^{18}				
PTAA(TPFB)	0	E_V+0.31	1.5×10^{13}	6.4×10^{12}	2.0×10^{12}	5.9×10^{12}	4.3×10^{16}	2.7×10^{16}	1.69	1.69
		E_V+0.43		2.2×10^{13}		1.4×10^{13}				
	10^{11}	E_V+0.31	3.2×10^{13}	5.0×10^{12}	7.7×10^{13}	4.2×10^{12}	6.7×10^{16}	4.4×10^{16}	1.65	1.66
		E_V+0.43		6.6×10^{13}		5.7×10^{13}				
	10^{12}	E_V+0.31	8.8×10^{13}	5.9×10^{12}	1.4×10^{13}	3.6×10^{12}	6.9×10^{16}	5.1×10^{16}	1.53	1.61
		E_V+0.43		1.4×10^{14}		1.1×10^{14}				
	10^{13}	E_V+0.31	1.5×10^{15}	3.4×10^{14}	2.9×10^{14}	1.7×10^{14}	3.0×10^{17}	2.8×10^{17}	1.40	1.51
		E_V+0.43		1.4×10^{15}		1.0×10^{15}				
PTAA(TPFB):C8BTBT(TPFB)	0	E_V+0.31	4.7×10^{12}		9.7×10^{11}		3.8×10^{16}	2.5×10^{16}	1.69	1.69
		E_V+0.43		3.7×10^{10}		1.6×10^{10}				
	10^{11}	E_V+0.31	6.4×10^{12}		2.1×10^{12}		7.7×10^{16}	4.6×10^{16}	1.66	1.68
		E_V+0.43		4.1×10^{11}		3.9×10^{11}				
	10^{12}	E_V+0.31	1.9×10^{13}		4.3×10^{12}		8.1×10^{16}	5.0×10^{16}	1.59	1.63
		E_V+0.43		2.3×10^{12}		1.5×10^{12}				
	10^{13}	E_V+0.31	9.2×10^{14}		3.6×10^{13}		1.4×10^{17}	8.9×10^{16}	1.48	1.57
		E_V+0.43		8.7×10^{12}		3.6×10^{12}				

* N_A refers to effective carrier density – upper limit for defect density

Table S6. Solar Cell parameters for the higher performing perovskite solar cells after 7 MeV proton irradiation and after additional thermal vacuum anneal

HTM	Accumulated Fluences (p/cm^2)	PCE (%)		V_{OC} (V)		FF (%)		J_{SC} (mA/cm^2)		R_S (Ω/cm^2)		R_{SH} (Ω/cm^2)	
		Post 7MeV	Post 7MeV + TV	Post 7MeV	Post 7MeV + TV	Post 7MeV	Post 7MeV + TV	Post 7MeV	Post 7MeV + TV	Post 7MeV	Post 7MeV + TV	Post 7MeV	Post 7MeV + TV
PTAA(TPFB):Spiro(LiTFSI)	0	16.3 ±1.0	10.1± 0.5	1.02± 0.03	0.91± 0.01	71.5 ±4.4	49.8± 2.2	22.4 ±0.2	22.3± 0.2	2.7± 0.6	4.8±2. 2	1343± 352	820±1 66
	10^{11}	16.2 ±1.3	9.3±0. 7	1.03± 0.05	0.89± 0.03	70.0 ±2.9	47.0± 2.0	22.4 ±0.2	22.3± 0.3	2.7± 0.6	5.0±3. 3	1201± 219	791±9 7
	10^{12}	12.3 ±1.3	6.4±2. 0	0.80± 0.02	0.72± 0.11	69.3 ±4.3	39.5± 6.6	22.1 ±0.7	22.2± 0.3	2.8± 0.8	5.9±2. 7	1292± 154	998±2 02
	10^{13}	7.8± 0.7	3.0±1. 0	0.70± 0.03	0.51± 0.08	51.5 ±3.1	26.8± 5.9	21.6 ±0.4	21.6± 0.3	1.7± 1.1	7.7±1. 4	670±9 2	574±1 84
PTAA(TPFB)	0	14.9 ±0.6	13.9± 1.7	1.08± 0.03	1.02± 0.01	61.8 ±4. 3	61.3± 6.7	22.4 ±0.2	22.2± 0.2	3.5± 1.6	3.8±2. 4	944±1 94	940±1 44
	10^{11}	13.7 ±0.7	16.4± 2.1	1.08± 0.03	1.07± 0.04	57.0 ±3.4	67.8± 6.6	22.3 ±0.1	22.6± 0.2	3.6± 0.5	3.9±1. 6	741±2 13	850±2 61
	10^{12}	12.1 ±0.5	14.9± 0.3	1.08± 0.04	1.07± 0.05	51.3 ±3.9	62.8± 2.9	22.2 ±0.2	22.3± 0.2	4.0± 1.1	4.2±1. 5	725±1 61	790±1 10
	10^{13}	8.5± 1.0	10.0± 0.5	0.90± 0.04	0.96± 0.05	48.5 ±4.4	53.0± 2.2	19.5 ±0.4	19.8± 0.4	7.6± 1.8	6.4±1. 5	486±4 8	602±3 4
PTAA(TPFB):C8BTBT(TPFB)	0	17.9 ±1.5	18.2± 1.4	1.06± 0.03	1.06± 0.03	74.0 ±4.1	75.3± 3.6	22.9 ±0.2	22.9± 0.2	2.6± 0.7	2.5±1. 2	1519± 371	1473± 326
	10^{11}	17.1 ±1.6	17.2± 1.6	1.05± 0.02	1.05± 0.02	71.8 ±6.0	72.3± 5.7	22.8 ±0.3	22.8± 0.3	2.8± 0.6	2.4±0. 3	1455± 109	1499± 185
	10^{12}	16.6 ±1.1	16.9± 1.3	1.04± 0.03	1.05± 0.03	70.8 ±3.9	71.8± 4.0	22.6 ±0.1	22.5± 0.1	3.4± 0.9	2.7 ±0.4	1084± 189	1192± 236
	10^{13}	10.3 ±0.2	11.9± 0.8	0.89± 0.03	0.94± 0.03	51.5 ±2.1	56.0± 4.2	22.5 ±0.1	22.7± 0.1	5.8± 1.2	4.9±1. 2	682±2 28	815±2 16

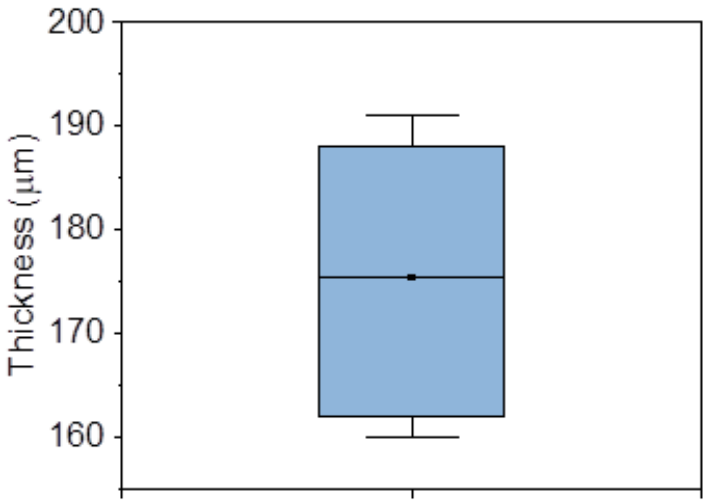

Figure S1 Thickness distribution of 16 sapphire substrates from the same batch. The thickness of 175±13 µm is close to the specified value.

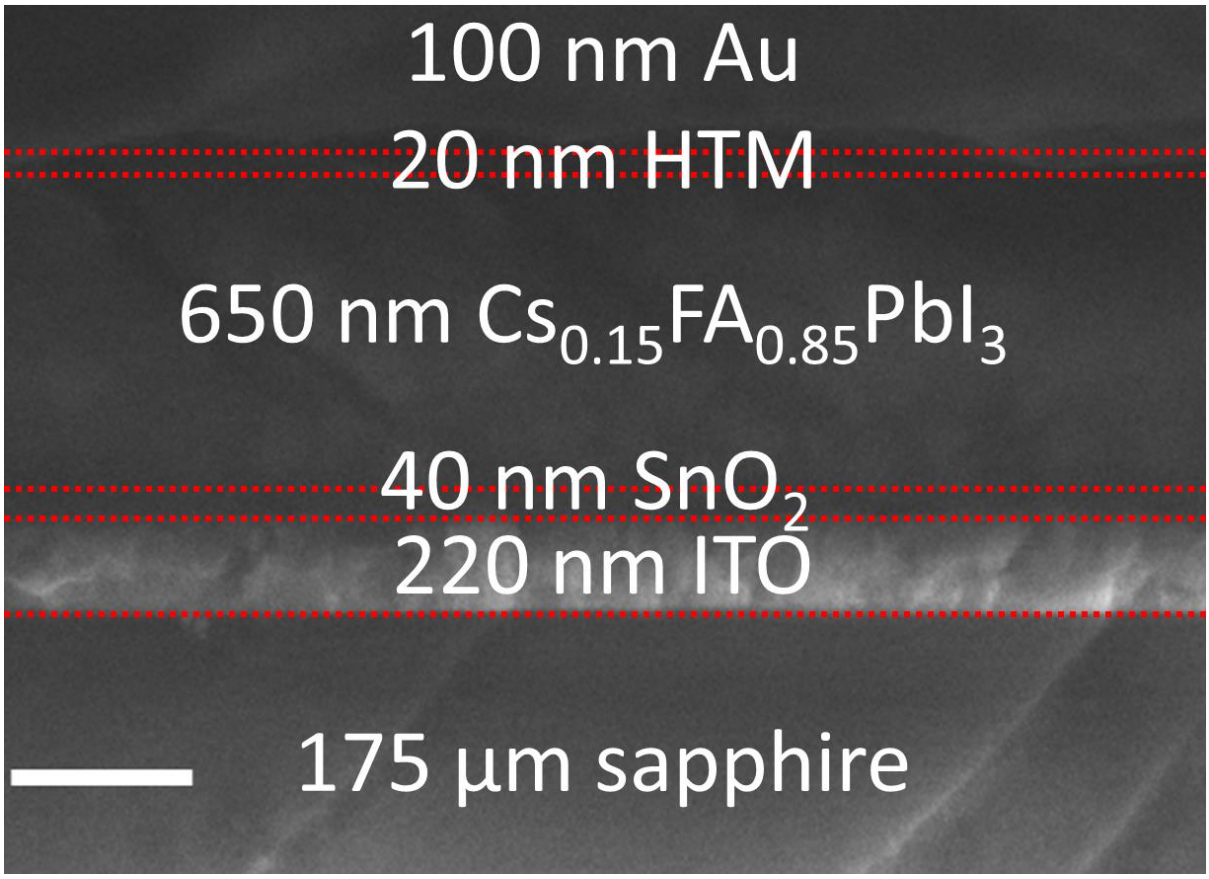

Figure S2 Cross-sectional scanning electron microscopy (SEM) image of a typical PSC fabricated in this work labelled with thicknesses. Scale bar = 400 nm.

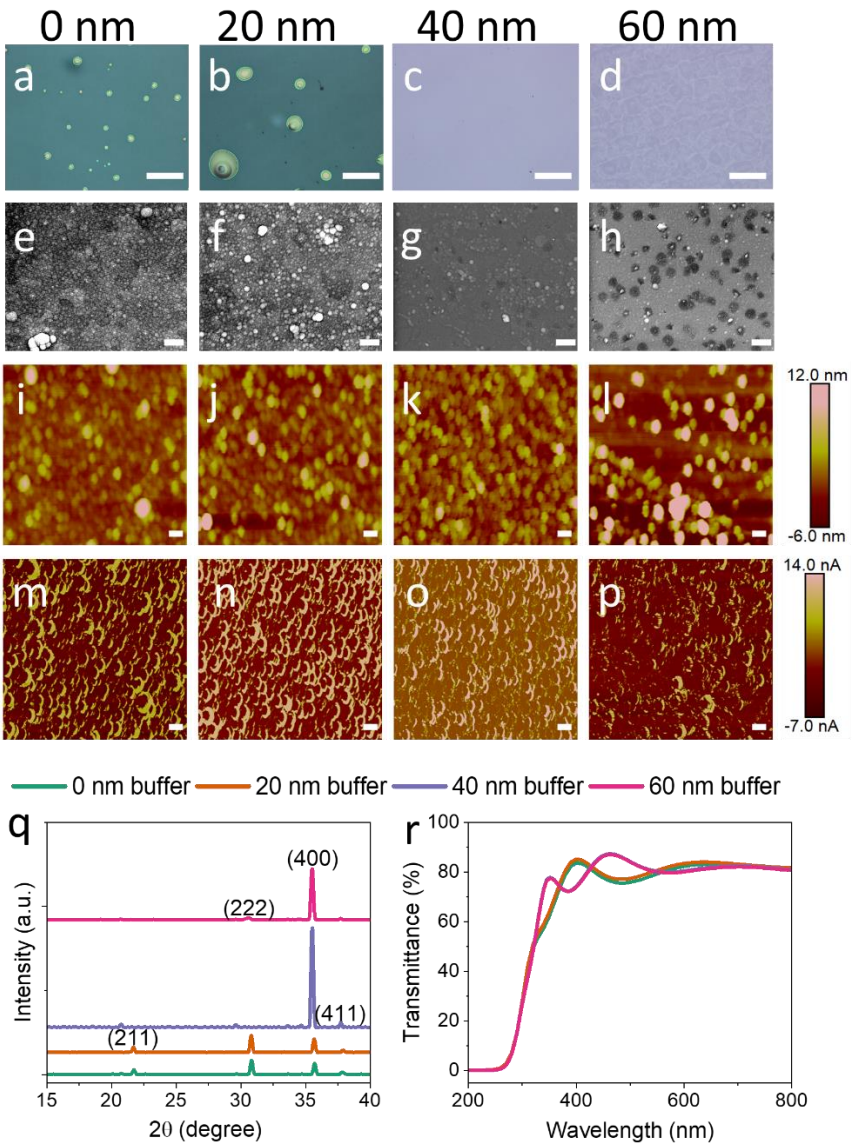

Figure S3. (a-d) Optical; (e-h) Top view SEM; (i-l) AFM and (m-p) Conductive-AFM images of ITO on 175-µm sapphire superstrate with varying underlying Al_2O_3 buffer layer thickness: (a, e, i, m) 0 nm; (b, f, g, n) 20 nm; (c, g, k, o) 40 nm and (d, h, l, p) 60 nm. Scale bars are 100 µm for optical images in (a) to (d) and 300 nm for other images (e) to (p). Pinhole formation and film non-uniformity can be observed in the ITO when the underlying Al_2O_3 thickness is below or above 40 nm. 60 nm Al_2O_3 results in slightly rougher film in the overlaying ITO according to AFM. 40 nm Al_2O_3 results in slightly smaller sheet resistance in the overlaying ITO according to c-AFM.

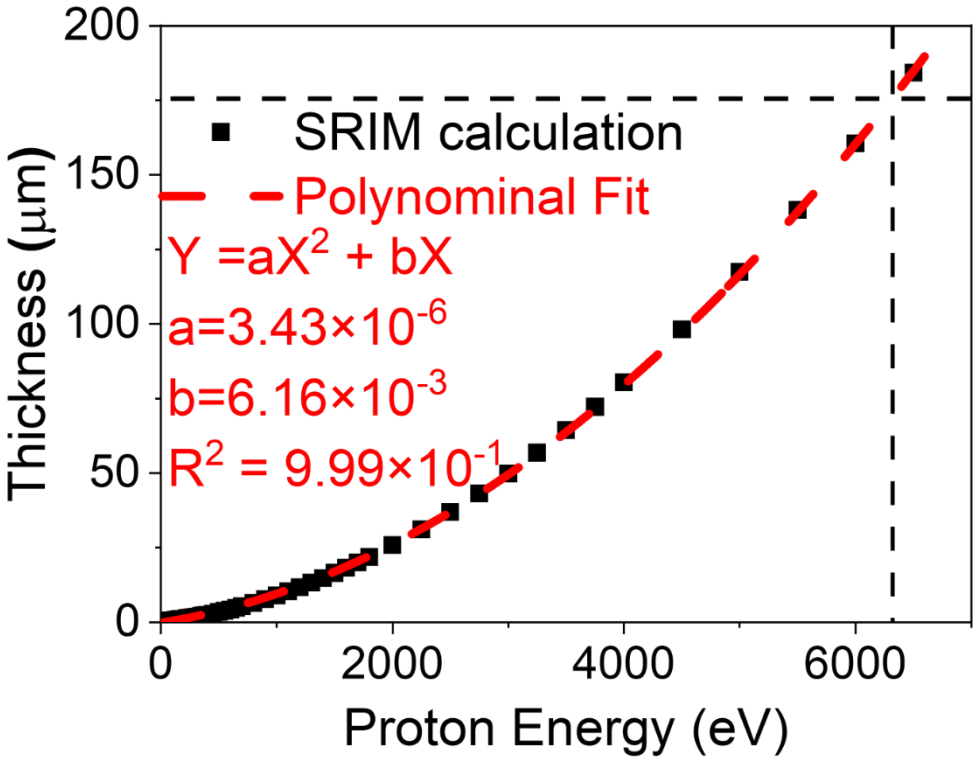

Figure S4. SRIM simulation to determine the proton energy that will penetrate through a 175-μm sapphire superstrate.

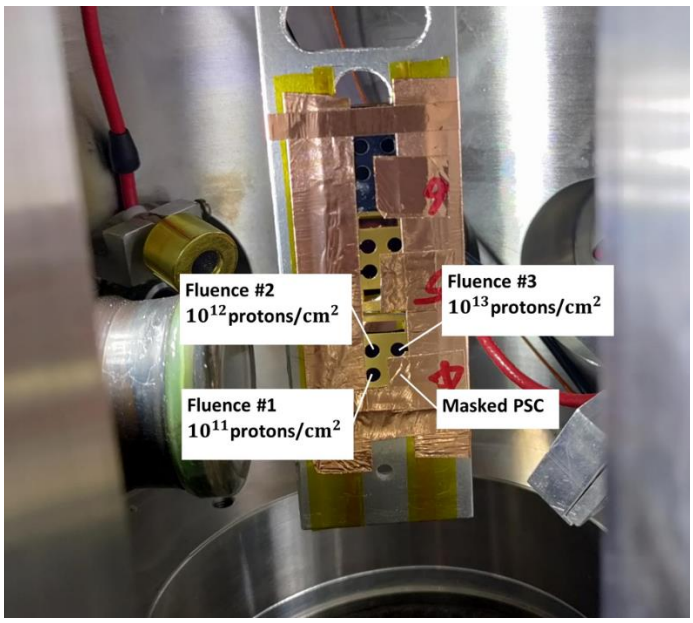

Figure S5. PSCs under test inside irradiation chamber exposed to 3 fluence levels through aperture or masked as control.

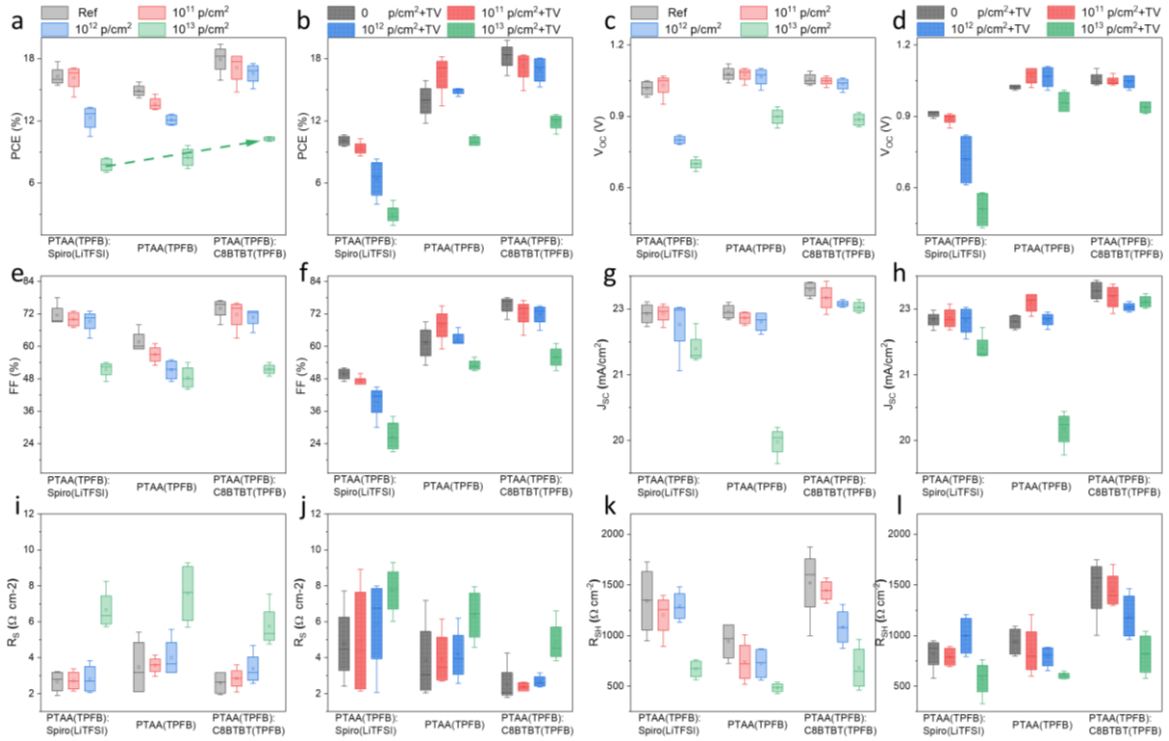

Figure S6. Distribution of (a,b) PCE, (c,d) V_{OC}, (e,f) FF, (g,h) J_{SC}, (i,j) R_S, (k,l) R_{SH} of i) PTAA(TPFB):Spiro(LiTFSI); ii) PTAA(TPFB); and iii) PTAA(TPFB):C8BTBT(TPFB) perovskite solar cells (a, c, e, g, i, k) before and after 7MeV proton radiations at 3 different fluences and (b, d, f, h, j, l) after additional thermal vacuum anneal

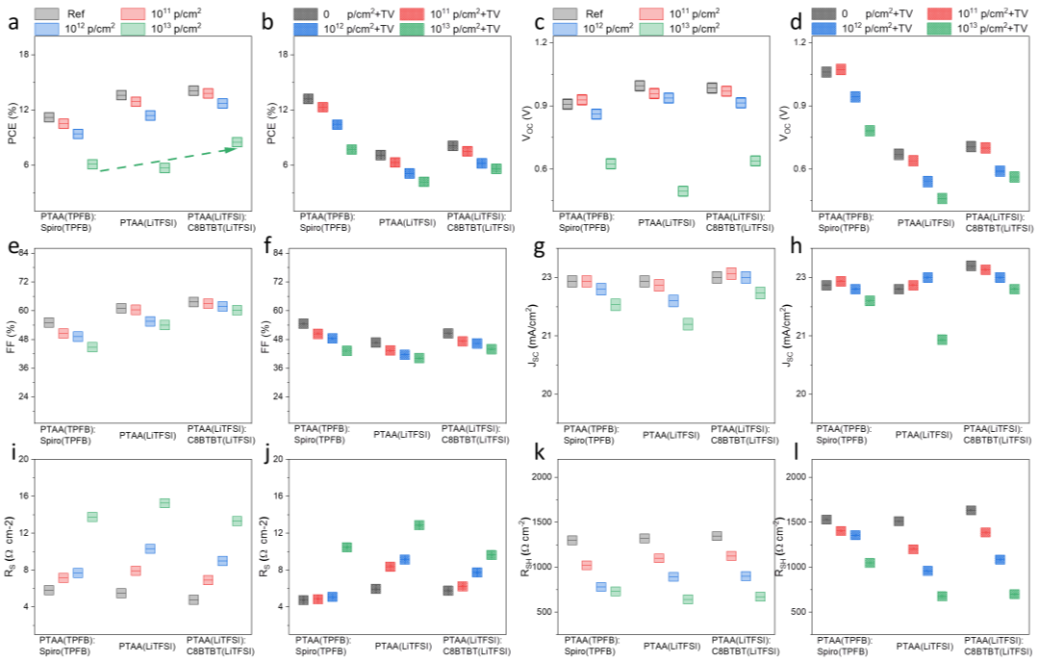

Figure S7. Distribution of (a,b) PCE, (c,d) V_{OC}, (e,f) FF, (g,h) J_{SC}, (I,j) R_S, (k.k) R_{SH} of i) PTAA(TPFB):Spiro(TPFB); ii) PTAA(LiTFSI); and iii) PTAA(LiTFSI):C8BTBT(TPFB) perovskite solar cells (a, c, e, g, i, k) before and after 7MeV proton radiations at 3 different fluences and (b, d, f, h, j, l) after additional TV

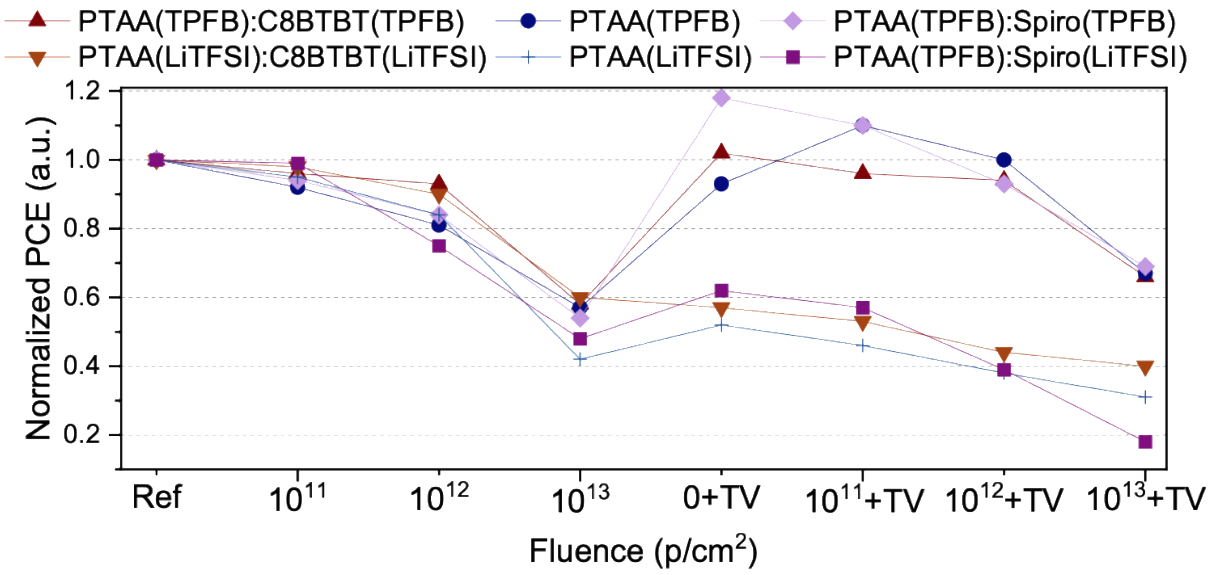

Figure S8. Evolution of average PCE, of all cell types before and after 7MeV proton radiations at 3 different fluences and after additional TV for the purpose of radiation hardness comparison.

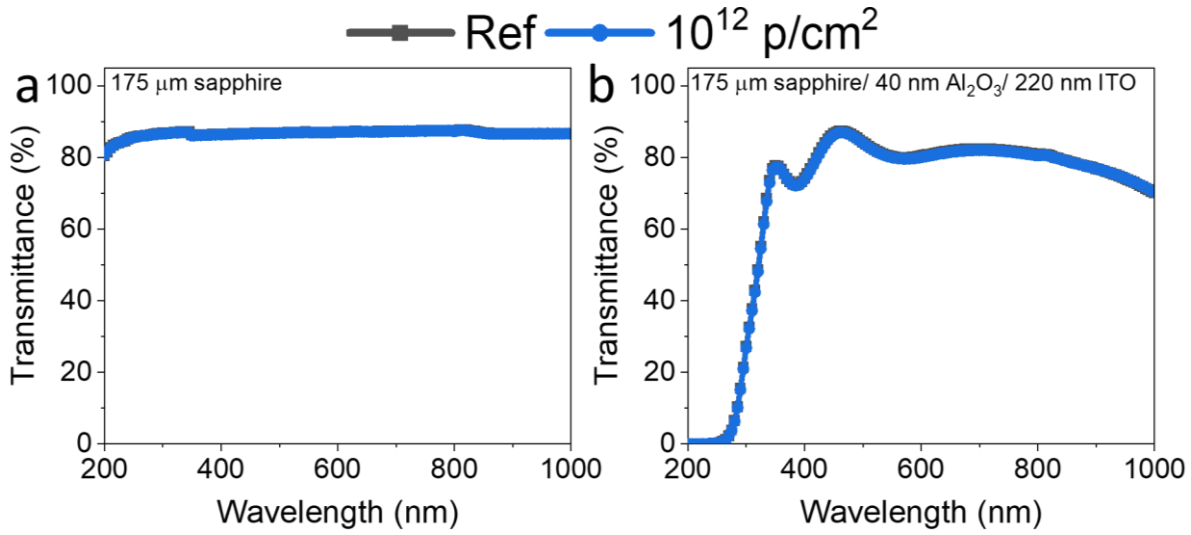

Figure S9. Transmittance of sapphire (a) without and (b) with the Al_2O_3/ITO layers before and after 7MeV 10^{12} p/cm^2 radiation showing no changes**.**

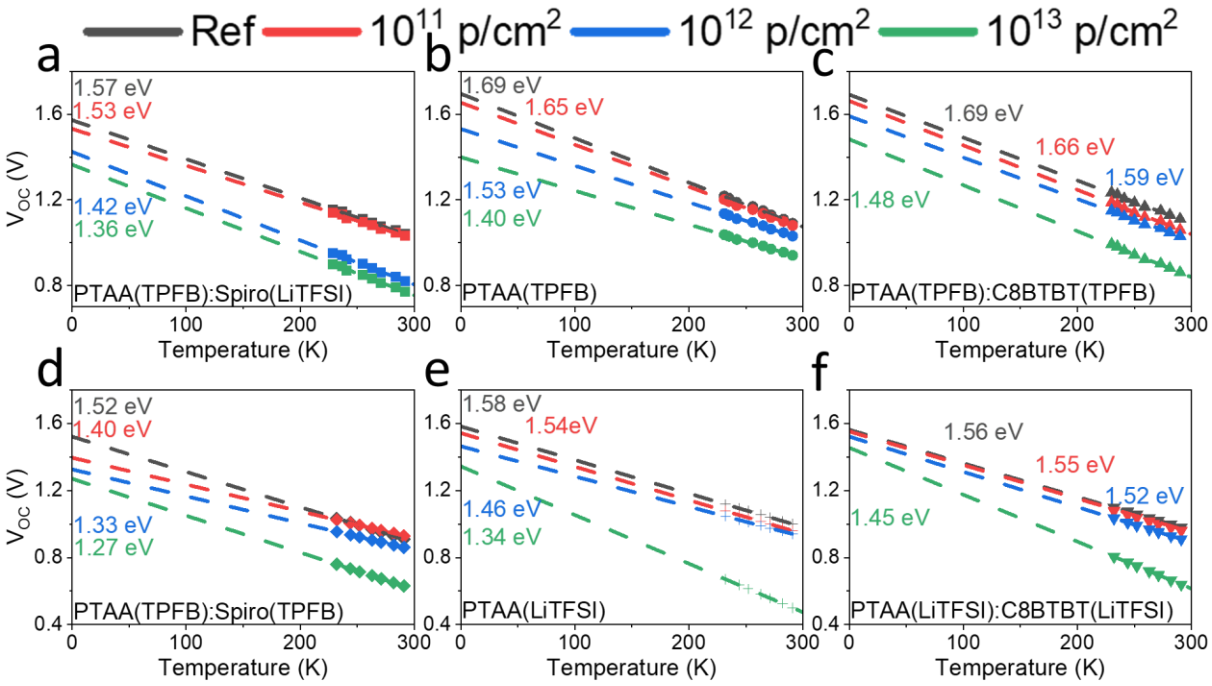

Figure S10. Temperature-dependent V_{OC} plot for determining the activation-energies (E_A) of recombination currents (y-axis intercept at 0K) for (a) PTAA(TPFB):Spiro(LiTFSI); (b) PTAA(TPFB); (c) PTAA(TPFB):C8BTBT(TPFB); (d) PTAA(TPFB):Spiro(TPFB); (e) PTAA(LiTFSI) and

(f) PTAA(LiTFSI): C8BTBT(LiTFSI) before and after irradiation with 7 MeV protons to10^{11}; 10^{12}; or 10^{13} p/cm^2

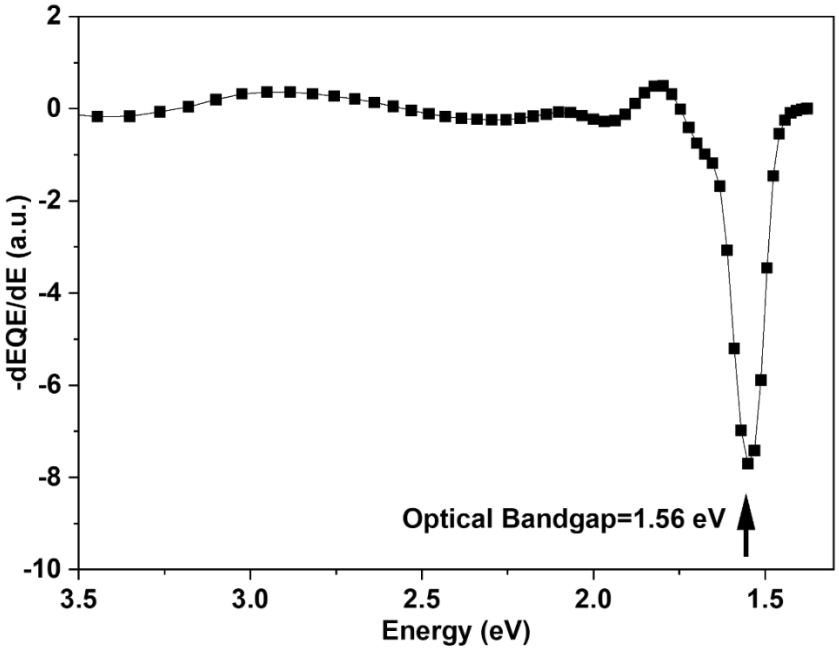

Figure S11. Typical bandgap of PSC fabricated in this work determined from measured external quantum efficiency (EQE) of one of the PSCs.

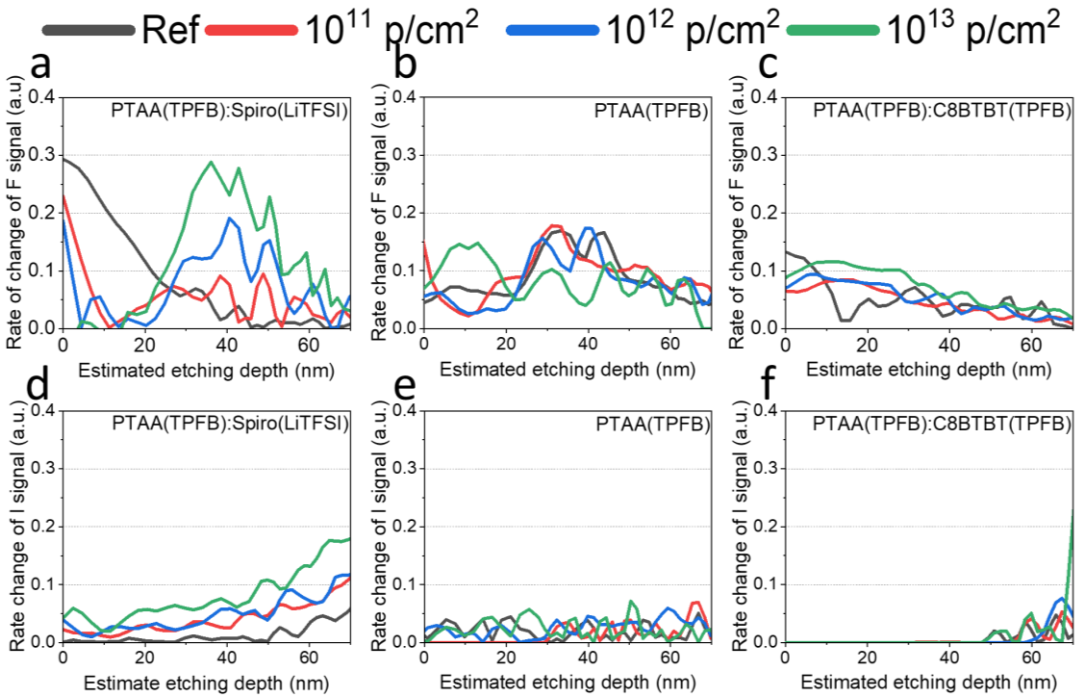

Figure S12. Rate of change for the (a, b, c) fluorine and (d, e, f) iodine XPS signals for (a,d) PTAA(TPFB):Spiro(LiTFSI); (b,e) PTAA(TPFB); and (c, f) PTAA(TPFB):C8BTBT(TPFB) before and after 7 MeV 10^{11}; 10^{12}; or 10^{13} p/cm^2 irradiation

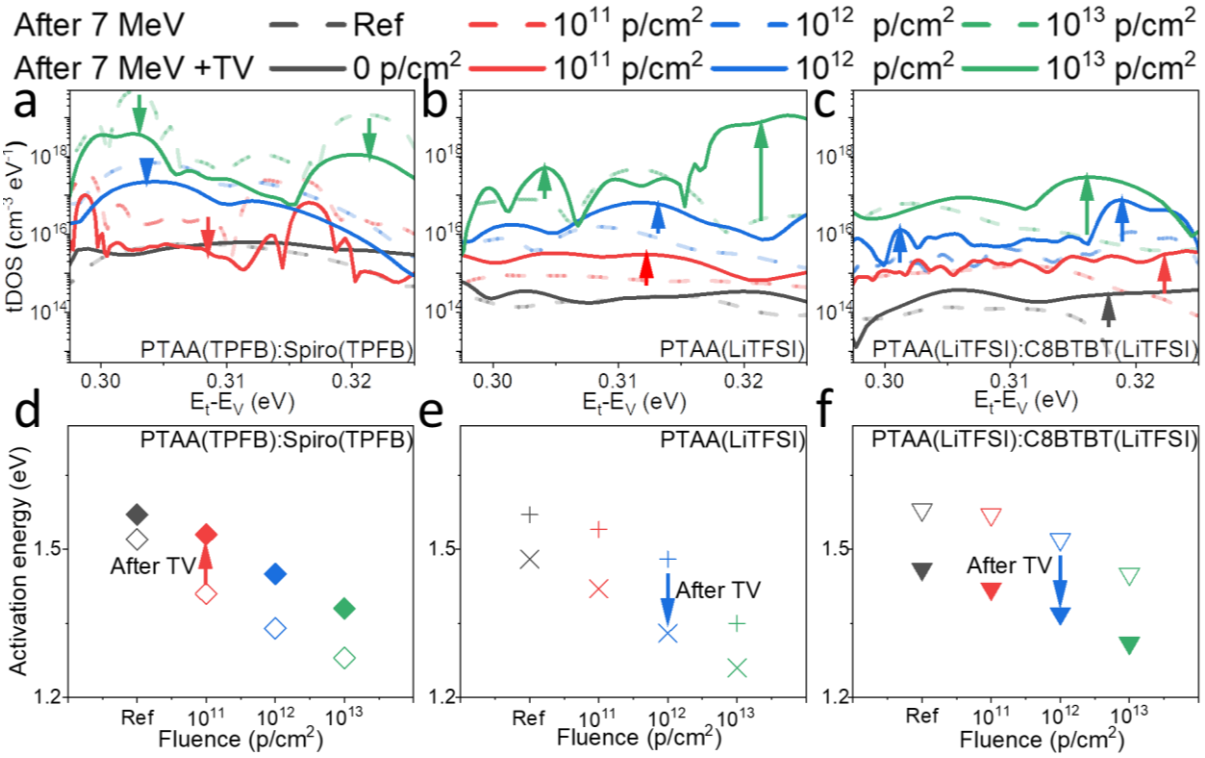

Figure S13 Effect of thermal-vacuum annealing on proton-irradiated lower performing (a, d) PTAA(TPFB):Spiro(TPFB); (b, e) PTAA(LiTFSI) and (c, f) PTAA(LiTFSI): C8BTBT(LiTFSI) cells. (a-c) thermal admittance spectroscopy, and (d-e) activation-energies E_A's 7MeV proton-irradiated cells before and after post thermal (80 °C for 30 mins) vacuum treatment.

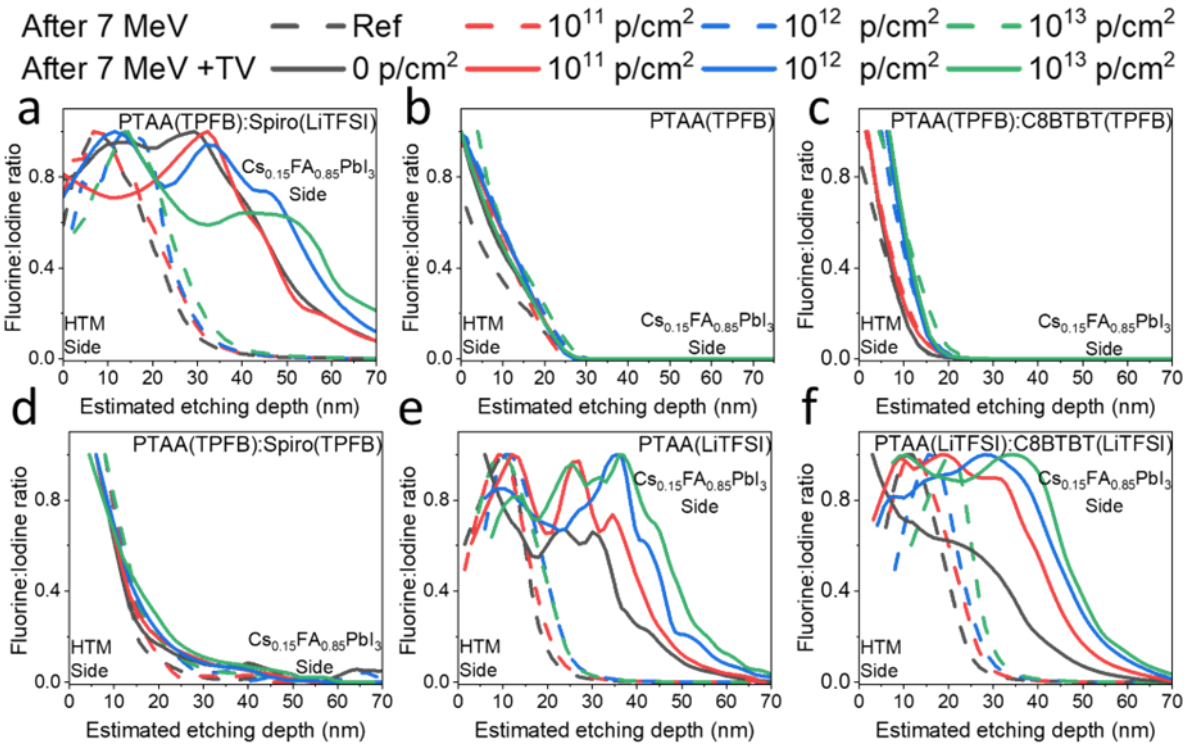

Figure S14. Atomic fluorine to iodine ratio as a function of estimated depth for (a) PTAA(TPFB):Spiro(LiTFSI); (b) PTAA(TPFB); (c) PTAA(TPFB):C8BTBT(TPFB); (d) PTAA(TPFB):Spiro(TPFB); (e) PTAA(LiTFSI) and (f) PTAA(LiTFSI):C8BTBT(LiTFSI) based PSCs after additional thermal (80°C) vacuum anneal (TV) compared to PSCs just after 7 MeV proton radiations.

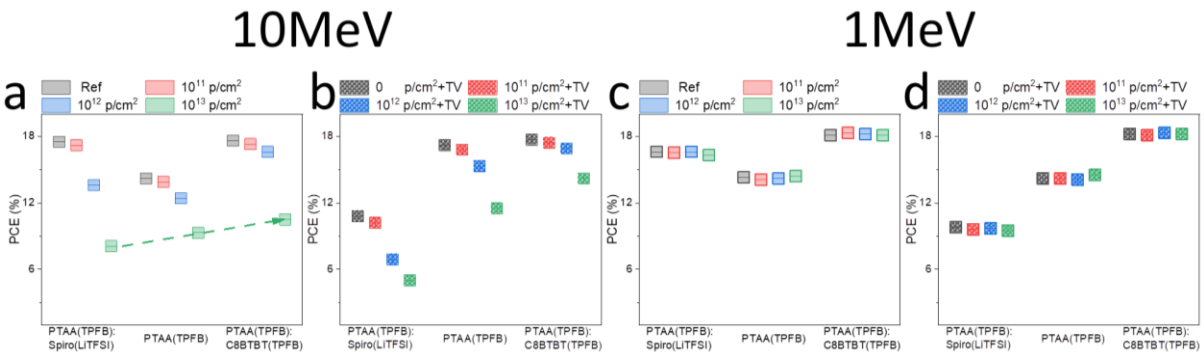

Figure S15. Distribution of PCE, for i) PTAA(TPFB):Spiro(LiTFSI); ii) PTAA(TPFB); and iii) PTAA(TPFB):C8BTBT(TPFB) perovskite solar cells before and after (a) 10MeV and (c) 1MeV proton radiations at 3 different fluences and (b, d) after additional TV

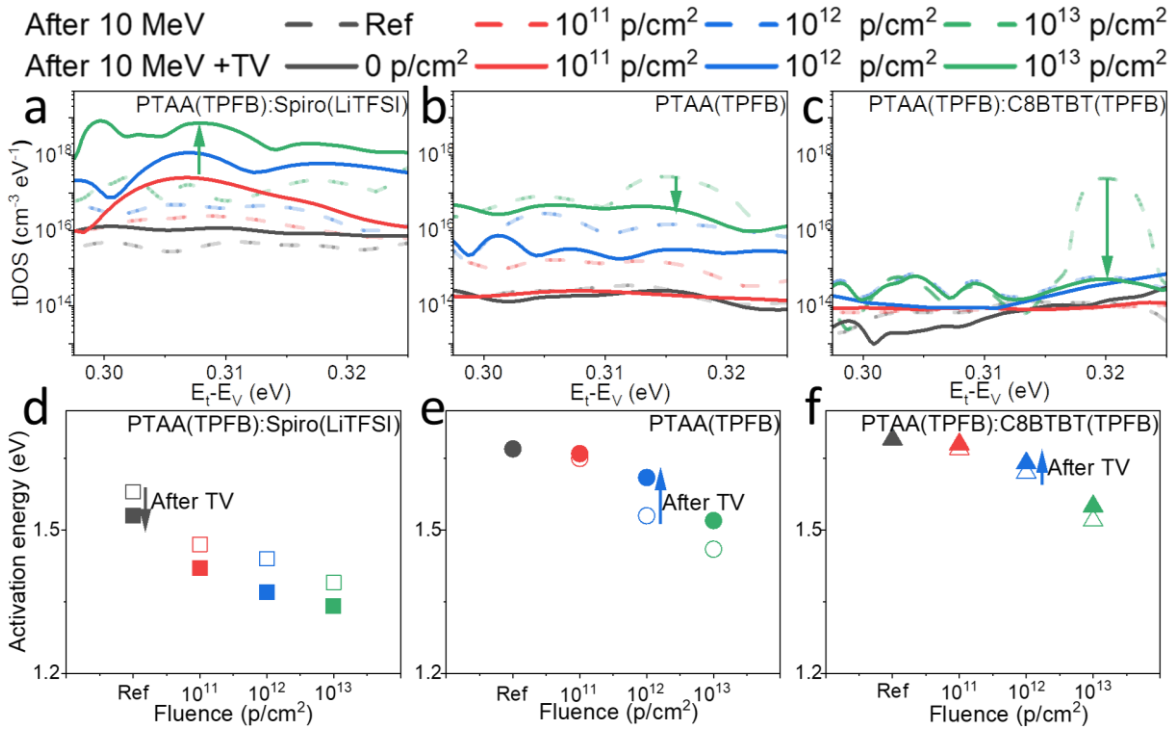

Figure S16 (a-c) thermal admittance spectroscopy, and (d-e) activation-energies E_A's 10MeV proton-irradiated (a, d) PTAA(TPFB):Spiro(LiTFSI); (b, e) PTAA(TPFB) and (c, f) PTAA(TPFB):C8BTBT(TPFB) cells before and after post thermal (80 °C for 30 mins) vacuum treatment.

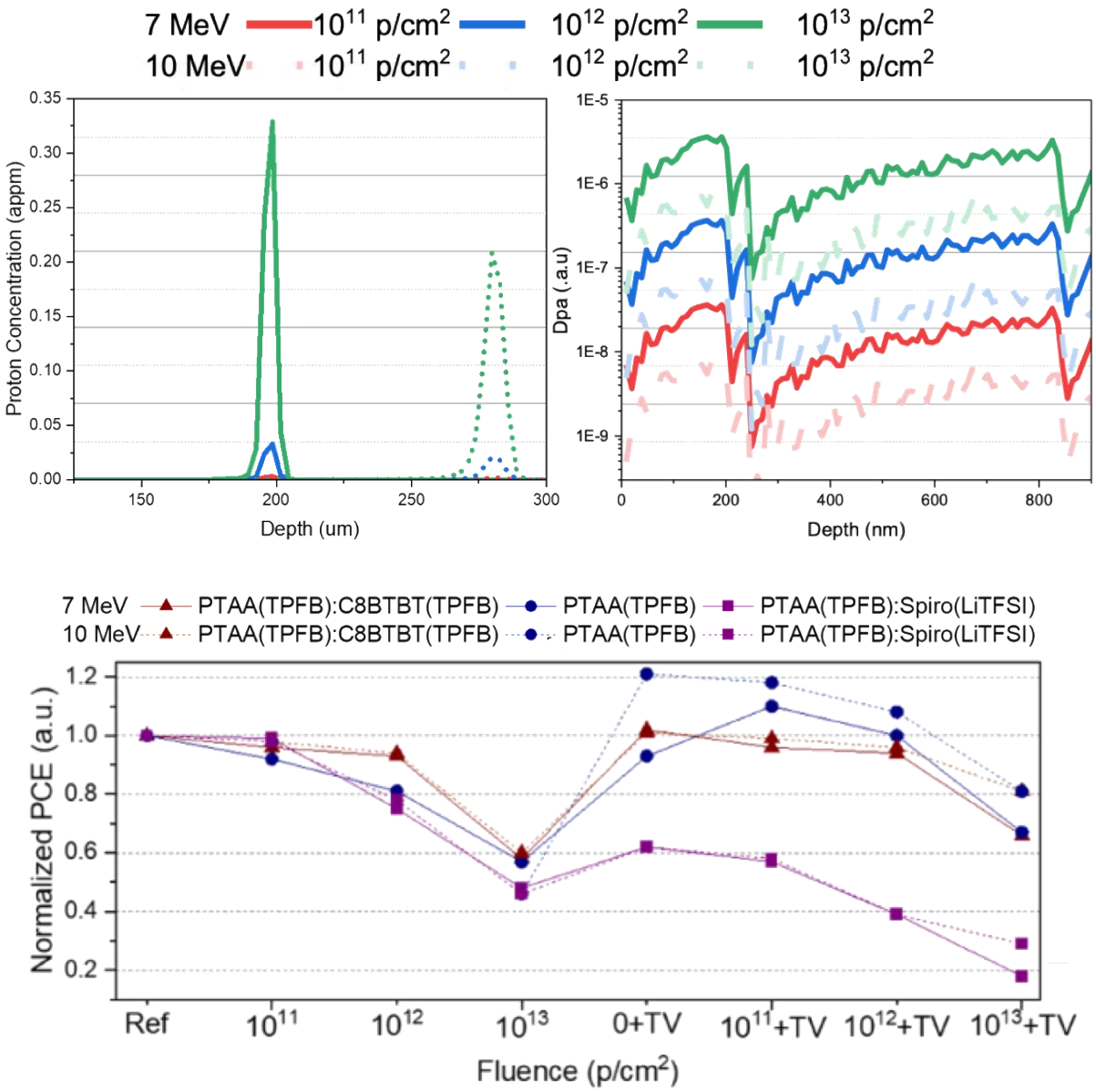

Figure S17. (a) Implanted 7MeV and 10MeV proton concentrations in atomic parts per million (appm) for a simulated imaginary cell with ~300 μm thick metal electrode in order to illustrate that the proton "stopping" peaks are well beyond the actual thickness of the solar cells (~1μm). (b) SRIM simulation of atomic displacement of a PSC by 7MeV and 10MeV protons under 3 different fluences. (c) Evolution of average PCE of i) PTAA(TPFB); and iii) PTAA(TPFB):Spiro(LiTFSI) perovskite solar cells before and after 7 MeV and 10 MeV proton radiations at 3 different fluences and after additional TV.

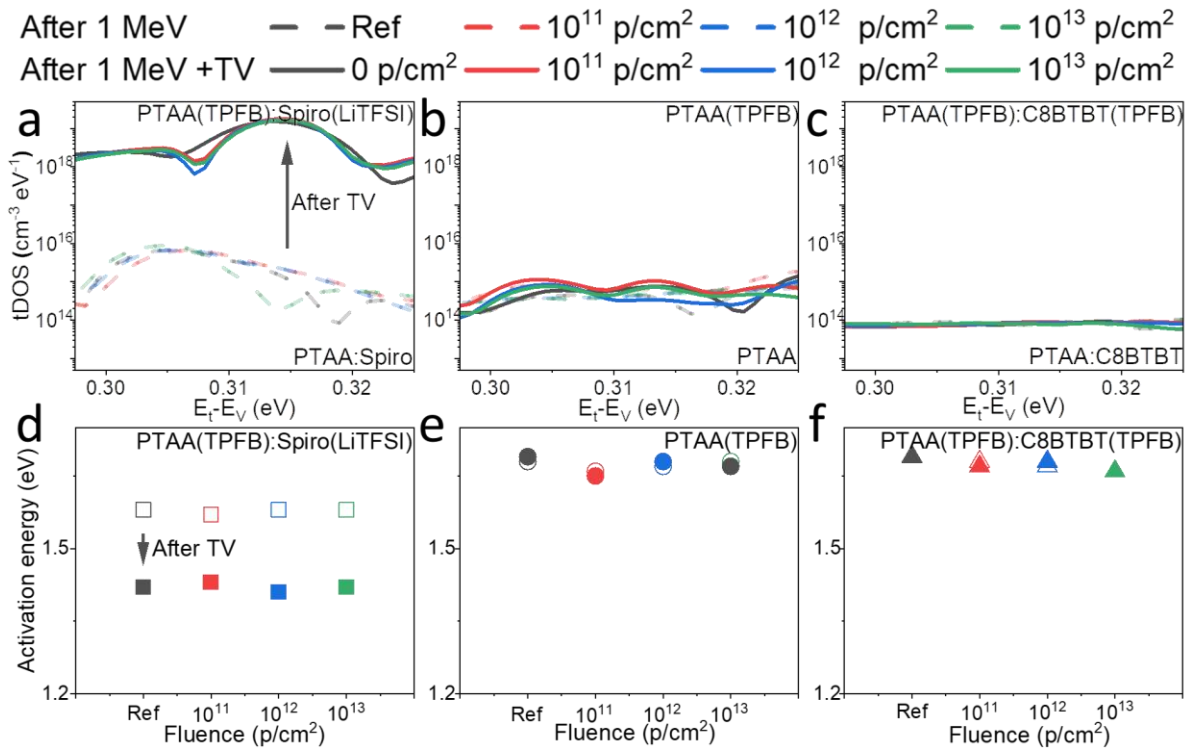

Figure S18 (a-c) thermal admittance spectroscopy, and (d-f) activation-energies EA's 1 MeV proton-irradiated (a, d) PTAA(TPFB):Spiro(LiTFSI); (b, e) PTAA(TPFB) and (c, f) PTAA(TPFB):C8BTBT(TPFB) cells before and after post thermal (80 °C for 30 mins) vacuum treatment.

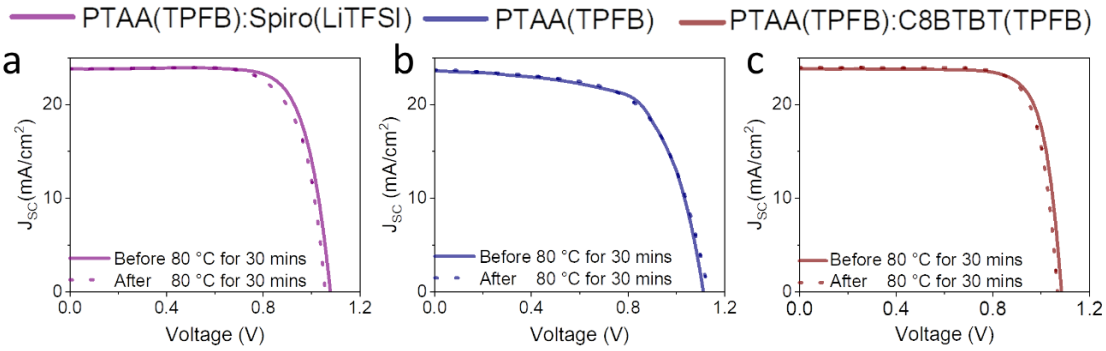

Figure S19. J-V characteristics of encapsulated (a) PTAA(TPFB):Spiro(LiTFSI); (b) PTAA(TPFB) and (c) PTAA(TPFB):C8BTBT(TPFB) PSCs before (solid) and after (dash) ambient thermal anneal (80°C for 30 mins).

Reference:

1. Miyazawa, Y.; Ikegami, M.; Miyasaka, T.; Ohshima, T.; Imaizumi, M.; Hirose, K. In *Evaluation of radiation tolerance of perovskite solar cell for use in space*, 2015 IEEE 42nd Photovoltaic Specialist Conference (PVSC), IEEE: 2015; pp 1-4.

2. Huang, J.; Kelzenberg, M. D.; Espinet-González, P.; Mann, C.; Walker, D.; Naqavi, A.; Vaidya, N.; Warmann, E.; Atwater, H. A. In *Effects of Electron and Proton Radiation on Perovskite Solar Cells for Space Solar Power Application*, 2017 IEEE 44th Photovoltaic Specialist Conference (PVSC), 25-30 June 2017; 2017; pp 1248-1252.

3. Miyazawa, Y.; Ikegami, M.; Chen, H.-W.; Ohshima, T.; Imaizumi, M.; Hirose, K.; Miyasaka, T., Tolerance of Perovskite Solar Cell to High-Energy Particle Irradiations in Space Environment. *iScience* **2018,** *2*, 148-155.

4. Barbé, J.; Hughes, D.; Wei, Z.; Pockett, A.; Lee, H. K. H.; Heasman, K. C.; Carnie, M. J.; Watson, T. M.; Tsoi, W. C., Radiation Hardness of Perovskite Solar Cells Based on Aluminum-Doped Zinc Oxide Electrode Under Proton Irradiation. *Solar RRL* **2019,** *3* (12), 1900219.

5. Kanaya, S.; Kim, G. M.; Ikegami, M.; Miyasaka, T.; Suzuki, K.; Miyazawa, Y.; Toyota, H.; Osonoe, K.; Yamamoto, T.; Hirose, K., Proton Irradiation Tolerance of High-Efficiency Perovskite Absorbers for Space Applications. *The Journal of Physical Chemistry Letters* **2019,** *10* (22), 6990-6995.

6. Xue, B.; Zhang, L.; Li, Z.; Jiang, W.; Liang, Y.; Liu, N.; Pan, C.; Chen, L.; Wang, T., Property degradation of mixed-cation perovskite films and solar cells irradiated with protons. *Nuclear Instruments and Methods in Physics Research Section B: Beam Interactions with Materials and Atoms* **2022,** *526*, 29-35.

7. Durant, B. K.; Afshari, H.; Singh, S.; Rout, B.; Eperon, G. E.; Sellers, I. R., Tolerance of perovskite solar cells to targeted proton irradiation and electronic ionization induced healing. *ACS Energy Letters* **2021,** *6* (7), 2362-2368.

8. Martínez, W. O. H.; Guerrero, N. B. C.; Andrade, V. A. G.; Alurralde, M.; Perez, M. D., Evaluation of the resistance of halide perovskite solar cells to high energy proton irradiation for space applications. *Solar Energy Materials and Solar Cells* **2022,** *238*, 111644.

9. Hughes, D.; Meroni, S. M. P.; Barbé, J.; Raptis, D.; Lee, H. K. H.; Heasman, K. C.; Lang, F.; Watson, T. M.; Tsoi, W. C., Proton Radiation Hardness of Perovskite Solar Cells Utilizing a Mesoporous Carbon Electrode. *Energy Technology* **2021,** *9* (12), 2100928.

10. Lang, F.; Nickel, N. H.; Bundesmann, J.; Seidel, S.; Denker, A.; Albrecht, S.; Brus, V. V.; Rappich, J.; Rech, B.; Landi, G.; Neitzert, H. C., Radiation Hardness and Self-Healing of Perovskite Solar Cells. *Advanced Materials* **2016,** *28* (39), 8726-8731.

11. Brus, V. V.; Lang, F.; Bundesmann, J.; Seidel, S.; Denker, A.; Rech, B.; Landi, G.; Neitzert, H. C.; Rappich, J.; Nickel, N. H., Defect Dynamics in Proton Irradiated CH3NH3PbI3 Perovskite Solar Cells. *Advanced Electronic Materials* **2017,** *3* (2), 1600438.

12. Lang, F.; Jošt, M.; Bundesmann, J.; Denker, A.; Albrecht, S.; Landi, G.; Neitzert, H.-C.; Rappich, J.; Nickel, N. H., Efficient minority carrier detrapping mediating the radiation hardness of triple-cation perovskite solar cells under proton irradiation. *Energy & Environmental Science* **2019,** *12* (5), 1634-1647.

13. Lang, F.; Jošt, M.; Frohna, K.; Köhnen, E.; Al-Ashouri, A.; Bowman, A. R.; Bertram, T.; Morales-Vilches, A. B.; Koushik, D.; Tennyson, E. M.; Galkowski, K.; Landi, G.; Creatore, M.; Stannowski, B.; Kaufmann, C. A.; Bundesmann, J.; Rappich, J.; Rech, B.; Denker, A.; Albrecht, S.; Neitzert, H.-C.; Nickel, N. H.; Stranks, S. D., Proton Radiation Hardness of Perovskite Tandem Photovoltaics. *Joule* **2020,** *4* (5), 1054-1069.

14. Lang, F.; Eperon, G. E.; Frohna, K.; Tennyson, E. M.; Al-Ashouri, A.; Kourkafas, G.; Bundesmann, J.; Denker, A.; West, K. G.; Hirst, L. C., Proton-Radiation Tolerant All-Perovskite Multijunction Solar Cells. *Advanced Energy Materials* **2021,** *11* (41), 2102246.